Computational Dissection of Two-Dimensional Rectangular Titanium Mononitride TiN: Auxetics and Promises for Photocatalysis

Liujiang Zhou,*,[†] Zhiwen Zhuo,[‡] Liangzhi Kou,[§] Aijun Du,[§] and Sergei Tretiak*,[†]

[†]Theoretical Division, Center for Nonlinear Studies and Center for Integrated Nanotechnologies, Los Alamos National Laboratory, Los Alamos, New Mexico 87545, United States

[‡]Department of Materials Science and Engineering, University of Science and Technology of China, Hefei, Anhui 230026, China

[§]School of Chemistry, Physics and Mechanical Engineering Faculty, Queensland University of Technology, Garden Point Campus, QLD 4001, Brisbane, Australia

Ⓢ Supporting Information

ABSTRACT: Recently, two-dimensional (2D) transition-metal nitrides have triggered an enormous interest for their tunable mechanical, optoelectronic, and magnetic properties, significantly enriching the family of 2D materials. Here, by using a broad range of first-principles calculations, we report a systematic study of 2D rectangular materials of titanium mononitride (TiN), exhibiting high energetic and thermal stability due to in-plane d−p orbital hybridization and synergetic out-of-plane electronic delocalization. The rectangular TiN monolayer also possesses enhanced auxeticity and

ferroelasticity with an alternating order of Possion's Ratios, stemming from the competitive interactions of intra- and inter- Ti—N chains. Such TiN nanosystem is a n-type metallic conductor with specific tunable pseudogaps. Halogenation of TiN monolayer downshifts the Fermi level, achieving the optical energy gap up to 1.85 eV for TiNCl(Br) sheet. Overall, observed electronic features suggest that the two materials are potential photocatalysts for water splitting application. These results extend emerging phenomena in a rich family 2D transition-metal-based materials and hint for a new platform for the next-generation functional nanomaterials.

KEYWORDS: Two-dimensional materials, titanium nitride, negative Possion's ratios, ferroelasticity, photocatalysis, first-principles calculations
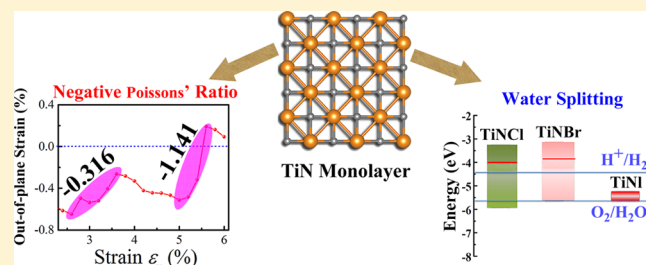
Transition metal dichalcogenides (TMDs) belong to a family of layered two-dimensional (2D) materials with promising potential applications, such as chip electronics, optoelectronics, catalysis, lubrication, superconductivity, and valleytronics.[1−3] Apart from tunability of bulk properties due to reduced dimensionality,[4] 2D TMDs are also known for a broad spectrum of polymorphic structures (i.e., 1T and 1H). Subsequently, they exhibit diverse properties that mostly depend on their composition and can be semiconductors (e.g., MoS_2, WS_2), semimetals (e.g., WTe_2, $TiSe_2$), true metals (e.g., NbS_2, VSe_2), and superconductors (e.g., $NbSe_2$, TaS_2).[5] Motivated by the successful development of 2D TMDs, 2D transition metal borides and nitrides followed with rich structural complexity and fascinating physical and chemical properties, thus substantially expanding the family of 2D TM-based materials. Among these systems, TM binitrites (such as YN_2,[6] MoN_2[7,8]) exhibit various useful functionalities due to the unsaturated N-2p orbitals. For example, this may introduce intrinsic magnetic properties and high capacity as electrode materials for metal ion batteries. Even though theoretical analysis predicts the ground-state of bulk MoN_2 to be a pernitride structure with the space group P63/mmc, importantly, pure layered MoN_2 materials with the rhombohedral (R3m) structure were successfully synthesized

recently.[9] Graphenylene-like MN_2 (M = Mo, W) monolayers are intrinsic quantum spin Hall insulators[10] further demonstrating the great feasibility of future applications.

In contrast to MoS_2-like MN_2 materials, 2D TM mononitrides (MNs) prefer alternative lattice configuration, namely, tetra-coordinated binding with neighboring TM atoms rather than the three-coordinated hollow lattice as seen in MN_2. Tetra-coordinated structures have been confirmed in NbN,[11] CrN,[12] ScN, and YN monolayers.[13] Rectangular form of NbN is shown to retain the metallic and superconducting (SC) properties of the bulk, whereas honeycomb form of NbN exhibits semiconducting electronic structure suitable for valleytronics, water splitting, piezoelectricity, and hot carrier solar cells.[11] The 2D ScN and YN nanosheets demonstrate indirect band gaps in the range of 0.6−2.2 eV and possess high visible light absorbancies.[13] Moreover, we previously reported existence of such lattice structures in MC (M = Ti, Zr, Hf),[14,15] TiNX (X = Cl, Br, I),[16,17] and TaCX.[18] These monolayers are predicted to have high structural stability

and pronounced quantum spin Hall effect. These findings underscore appearance of these 2D transition metal nitrides (especially mononitrides) phases with distinct properties from their bulk counterparts. For example, bulk MNs materials are well-known refractory compounds such as transition-metal monocarbides, showing a fascinating interplay of ionic, covalent and metallic bonding, which give rise to the high melting point and hardness.

In this Letter, we report first-principles calculations of rectangular titanium mononitride TiN monolayer. Our simulations suggest that TiN monolayer possesses unique mechanical properties, namely, auxeticity with very large negative Poisson's ratios (NPR) with the maximum value up to −1.141, an alternating order of Poisson's Ratio (+ − + − +) under a suitable external strain, and ferroelasticity (stress-induced switch of two lattice constants in the crystal structure) with an ultralow energy barrier for phase transition. Specific interaction between intra- and inter- Ti—N chains rationalizes the surprising NPR phenomenon. Although NPR are theoretically allowable, they are mainly observed in engineered materials and structures. The 2D nanomaterials with a NPR (auxetics) are extremely rare, and only several cases are reported, that is, phosphorene,[19] and δ-phosphorene,[20] monolayer SnSe,[21] borophane,[22] graphene and its nanoribbons,[19,23] pentagraphene,[24] Be_5C_2 monolayer,[25] penta-B_2N_4[26] and 2D silicon dioxide.[27] The 2D auxetics usually possess ferroelasticity,[22,28] leading to an unparalleled combination of such properties as high energy absorption and fracture resistance. Because the 2D TM-based auxetics is yet to be demonstrated, our modeling TiN monolayer facilitates experimental realization toward enriching the 2D auxetics family. We also show that TiN monolayer is the n-type metallic conductor and has a direct pseudogap. Its electronic features suggest the potential application to photocatalytic water splitting given upon functionalization. Overall such combination of these exceptional mechnical and optical properties implies potential application of TiN monolayers in the next-generation readable/writeable memory and optoelectronic technologies.

First-principles calculations based on the density functional theory (DFT) are carried out using the Vienna ab initio Simulation Package (VASP).[29] The exchange correlation interaction is treated within the generalized gradient approximation (GGA),[30] which is parametrized by the Perdew, Burke, and Ernzerhof (PBE).[31] Electronic wave functions were expanded in a plane wave basis set with a kinetic energy cutoff of 500 eV. All the atoms in the unit cell are fully relaxed until the force on each atom is less than 0.01 eV/Å. The reciprocal space was sampled with a k-grid density of 0.015 × $2\pi Å^{-1}$ for the structure optimization and 0.01 × $2\pi Å^{-1}$ for electronic SCF iterations using the Monkhorst−Pack method. Because DFT methods often underestimate the band gap, the screened exchange hybrid density functional by Heyd−Scuseria−Ernzerhof (HSE06)[32,33] is adopted to correct the PBE band gaps in the final calculations of the optimal structures. The phonon calculations are carried out by using the PHONOPY code.[34] The GW calculations, as implemented in BerkeleyGW package,[35,36] were performed without self-consistency in the Green's function and the screened Coulomb interaction (G0W0 approximation) in combination with the random phase approximation (RPA) or Bethe-Salpeter equation (BSE) calculations to calculate the quasi-particle band gap and the light absorbance with or without electron−hole (e-h) interactions. We calculated the dielectric matrix and the self-energy with a truncated Coulomb interaction[37] on a 20 × 16 × 1

k grid to converge our quasiparticle gap to within 0.1 eV. The number of bands was up to 10 times valence bands. The dynamical dielectric matrix was obtained via the random phase approximation (RPA) scheme and a generalized plasmon-pole model.[38] To carry out the BSE calculations within Tamm-Dancoff approximation, the matrix elements of BSE Hamiltonian were first calculated on a 20 × 16 × 1 k grid and subsequently interpolated on a finer 58 × 72 × 1 k-grid in which six valence bands and six conduction bands were included.

TiN can exist in two distinct 2D lattice forms, namely honeycomb and rectangular lattices, which are closely connected with [111] and [100] planes of its bulk rocksalt phase. The honeycomb TiN monolayer is assembled of [111] planar sublattices of [111] plane in the rocksalt structure of TiN and has a plane honeycomb lattice structure. Its phonon spectrum contains the unstable modes, implying that honeycomb lattice is dynamically unstable (Figure S1a,c). The relaxed atomically thin [100] plane of square TiN has a structure with quasisquare planar lattice (a = 4.091 Å, b = 4.127 Å). Its phonon spectrum also exhibits structural instabilities in the branch of acoustic phonons with an out-of-plane displacement (Figure S1b,d). We displaced atoms along the eigenvector of unstable mode at Γ-point and relaxed the structure to minimize the energy. In this cell-doubling distortion of the planar lattice, each formula unit of TiN displaces away from the other along z-direction.

Displacements of the Ti and N atoms in the relaxed structure can be envisaged as distortions off the quasisquare planar structure to an anisotropic puckered rectangular lattice form (see Figure 1a) in which each Ti atom is four-coordinated with
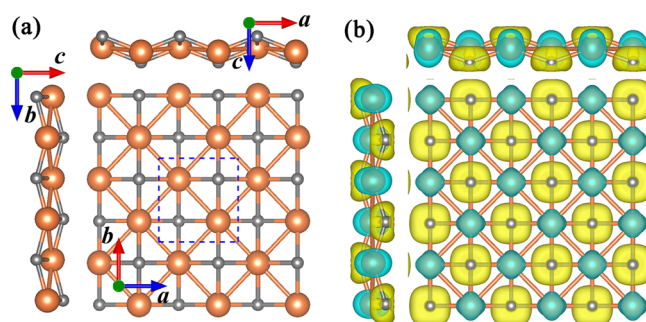
Figure 1. Structure of the TiN monolayer. (a) Atomic structure of sheet with two basic vectors **a** and **b**; the unit cell is indicated by blue dashed lines. (b) Isosurface plots (0.015 e/Å⁻³) of deformation electronic density. Charge accumulation and depletion regions are shown in yellow and blue, respectively.

ambient four N atoms. The rectangular TiN monolayer crystallizes in the orthorhombic lattice with space group *Pmmn*, showing the D_{2h} symmetry. TiN sheet has an anisotropic puckered rectangular structure with a thickness t = 1.24 Å. The lattice constants a and b are 3.716 and 3.945 Å (a/b ≈ 1.05), respectively, which is analogous to TiC[15] and NbN monolayers.[11] The buckling, measured by the spacing in the TiN bilayer, is 0.737 Å being slightly smaller than that in the transition-metal carbide monolayer MC (M = Ti, Zr, Hf).[14]

Phonon spectrum of rectangular TiN monolayer reveals no imaginary phonon modes (Figure S2), indicating that the rectangular phase form is kinetically stable. The highest frequency of the rectangular TiN monolayer reaches up to 620 cm⁻¹, close to the highest frequency of 580 cm⁻¹ in silicene[39] and higher than that of 473 cm⁻¹ in MoS_2 monolayer,[40] indicative of the robust Ti—N bonds in the rectangular structure. The energy

difference between the rectangular and hollow lattices reaches 0.433 eV/atom implying that the rectangular lattice has superior energetic stability and, therefore, higher experimental feasibility compared to the hollow structure. The ab initio MD simulations also demonstrate the thermal stability of TiN monolayer. As shown in Figure S3, the atomistic structures show no signs of a structural disruption below 2500 K prior to the melting at a temperature between 2500 and 3000 K, which is also higher than that observed in the transition-metal carbide monolayers MC (M = Ti, Zr, Hf), suggesting the high thermal stability of TiN monolayer. Thus, below we limit ourself by investigating TiN monolayer in a rectangular lattice.

The enhanced structural stability relates to the deformation electron density distribution. As shown in Figure 1b, the charge transfer occurs primarily from less electronegative Ti to the more electronegative N atoms. According to the Bader population analysis,[41] the net charger transfer from Ti to N is 1.48 electron per atom, that is, the TiN monolayer can be expressed as $Ti^{+1.48}N^{-1.48}$. The charge density plots in Figure S4a,b illustrate that this quantity is mainly distributed over N atoms, and the dumbbell shape of the N-p_z orbitals has the largest deformation spreading along the Ti—N bonds. To get deeper insight into the nature and stability of the bonding, we further analyze the electron localization function (ELF).[42] As shown in Figure S4c, the N-p_z orbitals shown in green (ELF = 0.50) imply heavily delocalized features. The blue contours around the Ti atoms (ELF = 0.00) indicate the electron deficiency of Ti atoms in the TiN monolayer, which agrees with the deformation electron density and Bader charge analysis.

The mechanical properties of the TiN monolayer, for example, curling resistance and endurance of the material to its own weight or external load, are characterized by the 2D Young's modulus Y_{2D}, calculated here to quantify in-plane stiffness. From the energy variations, subject to monoaxial strains (Figure S5), the Y_{2D}s along x- and y-axes are evaluated to be 0.127 and 0.329 TPa, respectively. These values are relatively smaller than that of graphene (1.0 TPa)[43] but comparable to MoS_2 (∼0.35 TPa)[44] and phosphorene figures (0.04−0.16 TPa).[45] On the basis of the elastic theory, we then check the deformation of rectangular TiN flake with one edge L fixed. By balancing gravity and 2D strain energy, the out-of-plane deformation h can be calculated with the expression $h/L \approx (\rho g L / Y_{2D})^{1/3}$,[46] where g and ρ are the gravitational acceleration and the density of the TiN monolayer, respectively. For a large TiN nanosheet of length $L \approx 100\,\mu m$, the ratio is $h/L \approx 10^{-4}$, indicating that the TiN monolayer is capable of being a free-standing membrane.

TiN monolayer belonging to orthorhombic crystal has four independent elastic constants: c_{11}, c_{12}, c_{22}, and c_{66}. Our calculations estimate $c_{11} = 48.63$ N/m, $c_{12} = 70.59$ N/m, $c_{22} = 133.57$ N/m, and $c_{66} = 53.22$ N/m. These c_{ij} constants are substantially smaller than those of graphene (∼340 N/m[43]) but comparable to silicene (62 N/m[47]) and phosphorene (24−103 N/m).[46] Intriguingly, the ratio of $c_{12}/c_{11} > 1$ is indicative of the potential feasibility of the out-of-plane negative Poisson' ratios (NPR). To verify this conjecture, we proceed to assess its structural response to the uniaxial strain. The calculated resultant strain in the range of ±10% tension applied along the x- or y-direction, is presented in Figure 2. We observe that a uniaxial strain in the x- (y-) direction induces an almost linear strain response in the y- (x-) direction near the equilibrium configuration. In contrast, the out-of-plane strain along z-direction demonstrates very exotic opposite response to the tensile (compressive) strain along x- (y-) direction persisiting in
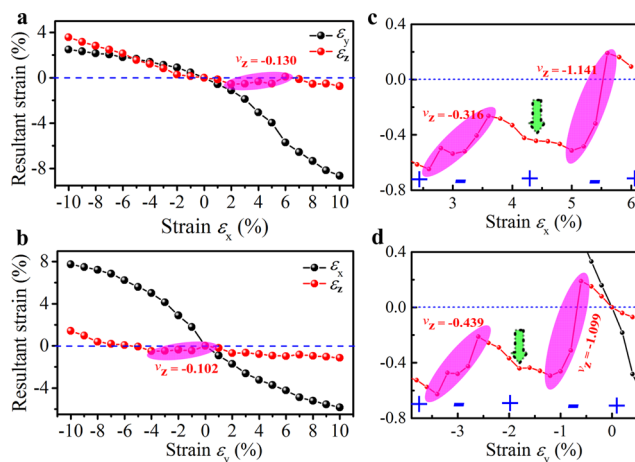

Figure 2. Resultant strain induced by the uniaxial strain along x- (a), and y- (b) directions. The strain range with negative Poisson's ratio are marked in pink ellipses. The negative Poisson's ratio is obtained by a linear fitting procedure. (c,d) The zoom-in resultant strain in pink oval-shaped range subject to the external strain along x- and y-axes, respectively. The green arrows indicate the strains where a switch of lattice occurs.

some range. This demonstrates the NPR in the out-of-plane direction. With a small magnitude of uniaxial strain, the first-order NPR approximation yields, $\nu \approx -\frac{\Delta L'}{\Delta L}$ where $\Delta L'$ is the lattice constant variation and ΔL is the layer thickness variation upon applied external strain. In the pink-elliptic regions (i.e., 2−6% and −4−0% strains for x- and y-axes, Figure 2), we estimate the NPR to be −0.130 and −0.102 when applying stretching and tensile strains along x- and y-directions, respectively. Because the lattice constant and thickness variations would be less precise in such extended strain range, we zoom-in the two NPR ranges by calculating the strain response on much denser strain points. Figure 2c shows that the out-of-plane strain response is more sensitive to the external strains and, moreover, it reveals the alternative positive−negative−positive−negative−positive (+ − + − +) ordering for the Poisson' ratios. In the case of stretching strain along x-direction, we observe two extremely large NPRs up to −0.316 and −1.141 in the ranges of 2.6−3.6% and 5−5.6%, respectively. The out-of-plane strain with respect to the tensile strain along y-direction also yields the similar alternating order (+ − + − +) for the Poisson' ratios (Figure 2d) with the two largest NPR −0.439 and −1.099 in −3.4 to −2.6% and −1.2 to −0.6% ranges, respectively.

These results establish TiN monolayer as a novel 2D material exhibiting pronounced NPR properties. Notably, calculated TiN NPRs compare well to other 2D materials, such as graphene (−0.33)[19] and its derivitives [such as semifluorinated graphene (−0.03 to −0.053)[48]], phosphorene (−0.027),[19] borophane (−0.053),[22] Be_5C_2 monolayer (−0.041 to −0.16)[25] and silicon dioxide (−0.022 to −0.123).[27] Trends similar to other materials with respect to the applied in-plane strain indicate existence of a lattice switch at 4.4% or −1.8% strain, implying ferroelasticity in TiN monolayer.

To probe the origin of the NPR, we further analyze the associated structural response (i.e., variations of bonding lengths, bonding angles, and atomistic height) in TiN monolayer. The lattice is comprised of two Ti—N chains linked by intra- and interchain Ti—N bonds. To connect the anisotropic strain response and the NPR, the stress-induced changes in out-of-plane thickness was decoupled into two parts, that is, the
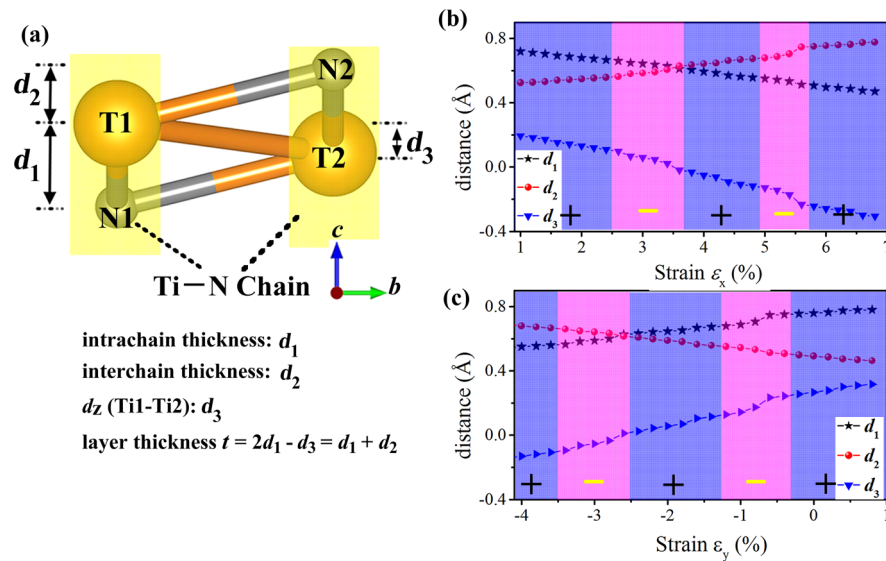
Figure 3. (a) Top: Schematic diagram of the Ti−N chains in the unit cell. Bottom: bonding parameters, intrachain height (d_1), interchain height difference (d_2), and vertical height difference within two Ti atoms (d_3), subject to tensile strain along x-direction and compressing strain along y-direction. The elongations (shrinks) of length or height are indicated by blue (red) arrows. The variations of d_1, d_2, as well as d_3 under a strain deformation along x- (b) and y- (c) directions, respectively.

intrachain height d_1 between T1 and N1 (or between T2 and N2) atoms and the interchain height d_2 between T1 and N2 (or between T2 and N1) atoms (Figure 3a). The layer thickness is given by $t = d_1 + d_2 + 2r_{vdw(N)}$, where $r_{vdw(N)}$ is the van der Waals radius of N atom set to 1.55 Å. Upon applying strain, the relative movement of two chains lead to a spontaneous local dislocation of two Ti atoms, which could be measured by the vertical height difference d_3 of two Ti atoms. Thus, the thickness t could also be calculated as $t = 2d_1 - d_3 + 2r_{vdw(N)}$. When stretching (compressing) lattice along x- (y-) direction, d_1 would decrease (increase) monotonically whereas d_2 vary in an inverse way. Consequently, the variation of layer thickness t depends on the competition of intra- and interchain interactions. For example, upon stretching lattice along x-direction in the 2.6−3.6% range, the d_1 increase is larger than the d_2 decrease, leading to a thicker t and, thus, to the NPR emergence. In contrast, in the 3.6−5% strain range, the thickness t reduces because the d_1 rise gradually saturates and is unable to compete with the d_2 decline. There trends are clearly manifested by the slope values for the d_1 and d_2 variations (Figure 3b). Similar analysis can be done for d_1 and d_3 variables: the NPR appears when the decrease of d_3 is faster than the increase of d_1. Noticeably, the lattice orientation switches at 4.4% strain (critical point) due to the close lattice constant a and b (Figure 2c). Further application of the stretching strain leads to reoccurrence of the NPR effect in the 5−5.6% range. These strain-induced variation of Possion's Ratios have alternating signs (+ − + +) when stretching lattice. The structural response to the tensile strain along y-direction could be analyzed as well, as shown in Figure 3c.

As exemplified by other 2D materials, ferroelasticity may exist in a 2D auxetics. We further seek the strain-induced structural transition by analyzing the energy variation under the tensile and compressive strains along x- and y-axes, respectively (Figure S6). An increase (decrease) of strain induces a contraction (an expansion) in the y- (x-) direction, drawing closer the nearest Ti and N atoms toward generating the new Ti−N bonds in the y- (x-) direction. This results in a switch of lattice orientation at 6.2% (−5.8%) strain. When tensile (compressing) strains are in the x-

(y-) direction, the total energy quadratically increases with strain within the elastic region up to a critical strain of 3.6% (−2.6%). Beyond this point, the energy drops in a reversed quadric way to an alternative minimum at almost the same energy, adapting geometry with opposite lattice constants a and b, which further indicates the lattice switch. The total activation barrier for TiN monolayer is calculated to be small (0.8 meV/atom). Larger values were reported for SnSe (1.3 meV/atom),[28] GeS (22.6 meV/atom), GeSe (9.8 meV/atom), SnS (4.2 meV/atom),[28] phosphorene (0.2 eV/atom),[19] and borophane (0.1 eV/atom)[22] monolayers. Hence, the ferroelastic switching are feasible at low temperatures because the lattice constants a and b are much closer to one another in TiN. The similar alternating Possion's Ratios and ferroelasticity are also observed when compressing the TiN lattice along the y-direction.

We next change our discussion from mechanical to electronic properties of TiN monolayer. The band structure calculated with PBE functional is shown in Figure 4a. Considered TiN monolayer shows metallic features and is expected to be a n-type metallic conductor. The bottom of the conduction band (CB) resides slightly lower the Fermi level E_F, and a visible band gap (a pseudogap) of 1.28 eV is noticeable. The charge distributions around the pseudogap (points A and B) in TiN monolayer are different as illustrated by real-space orbital plots (Figure 4b) and the projected density of states (Figure 4c,d). At the point A, Ti-d orbitals are heavily mixed with N-p orbitals, which are partially delocalized over the Ti−N bonds (Figure 4b). The delocalized states mainly arise from N-p_z orbitals hybridized with d_{xy} and d_{z^2} orbitals of Ti atoms (Figure 4c,d). This is crucial in stabilizing the quasi-planar tetra-coordinated N atoms in terms of passivating out-of-plane bonds and strengthening in-plane Ti−N bonds, in analogy to that in TiC sheet.[15] The orbitals above the pseudogap (point B) are mainly composed of the Ti d-orbitals, where we can clearly distinguish participation of the d_{xy} orbitals spreading in the $x−y$ plane in real place (Figure 4b), fully compatible with the square lattice symmetry and suggesting $d_{xy}−d_{xy}$ interactions. This potentially can lift the localization of d-band electrons toward extended Ti−
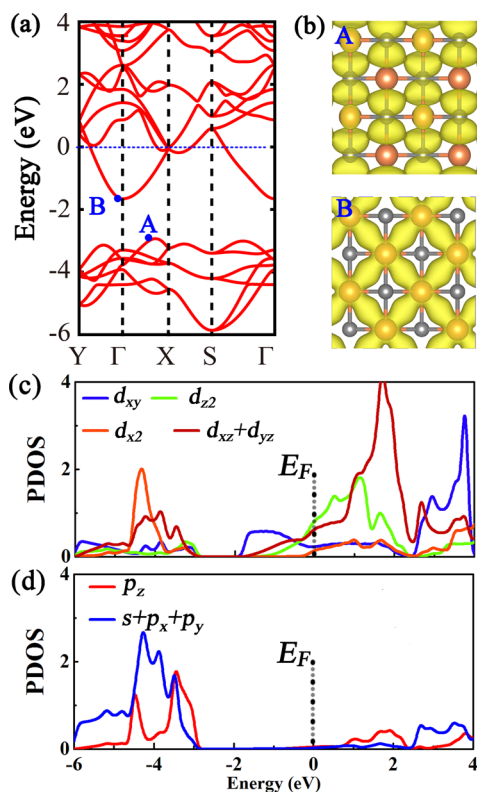
Figure 4. (a) Band structure of TiN monolayer. Γ, Y, X, and S correspond to the (0, 0, 0), (0, 0.5, 0), (0.5, 0, 0), and (0.5, 0.5, 0) k-points in the first Brillouin zone, respectively. (b) Isosurface (0.1 e/Å^{-3}) of partial charge densities at A (upper) and B (lower) points in (a) plot. (c,d) Projected density of states (PDOS) of TiN monolayer. The Fermi level is set to zero.

Ti bonds, leading to the nonmagnetic ground states, which was also verified by the calculated orbital moment of 0 μB from a spin-polarized ab initio calculations.

The n-type metallic conductance and the pseudogap of TiN monolayer suggest potential application in optoelectronic devices upon lowering the Fermi level within the pseudogap to achieve the real energy gap system. Chemical functionalization is an efficient approach for modulating the Fermi level. Considering the large electronegativity of halogen atoms, we further introduce these atoms into our TiN monolayer. Here we mainly consider two halogen atoms per unit cell adsorbed on both sides of TiN monolayer so as to resemble the most stable 2D TiNX (X = Cl, Br, I) crystals that could be stacked up into the 3D bulk phases of α-type TiNX (already synthesized in experiment[49]) via weak van der Waals interaction interaction. Viable adsorption sites for halogens on the TiN sheet are on the

top of N (T_N) or Ti (T_{Ti}) atom. For example, in the case of Cl functionalization, T_N adsorption is more stable by some 0.12 eV per unit cell compared to that on T_{Ti} site. To assess the adsorption strength, the adsorption energies were calculated as defined below

$$E_{ad} = \frac{(E_{TiNX} - E_{TiN} - 2E_X)}{2} \qquad (1)$$

where E_{TiNX} and E_{TiN} are the total energies of TiNX and TiN monolayers, respectively, and E_X is the total energy per atom of X$_2$ molecular. The calculated adsorption energies E_{ad} are −2.57, −2.19, and −1.58 eV/atom for TiNCl, TiNBr, and TiNI monolayers, respectively. Such large adsorption energies indicate the strong strength of adsorption. Luckily, the finally stable geometries with halogen atoms adsorbed on T_N sites are exactly those monolayers within 3D layered bulk phases of TiNX.[17] Thus, the obtained TiNX monolayer possess a high feasibility of experimental access via simple chemical exfoliation from corresponding 3D bulk phases. We next focus our attention on electronic and optical properties of stable TiNX monolayer. TiNX has reduced a and expanded b lattice parameters compared to its pure TiN counterpart (Table 1). The calculated band structures in Figure S7 clearly demonstrate that halogenation downshift the Fermi level. For example, we calculate the energy gaps of about 0.49 (0.48) eV (PBE) or 1.41 (1.39) eV (HSE06) for the TiNCl(Br) monolayer, which suggest potential applications in photovoltaics or photocatalysis for these materials. In contrast, the TiNI monolayer exhibits a semimetal feature with the appearance of a Dirac cone centered at finite momenta on Y-G-Y points in the 2D Brillouin zone in the absence of spin−orbital coupling (SOC) (Figure S7c). Previous computational study[16] reported that TiNI monolayer is an intrinsic quantum spin insulator with a small energy gap when SOC is included. Thus, we further consider only TiNCl and TiNBr monolayers.

To account for enhanced electron−hole interactions and reduced charge screening effects in our low-dimensional systems, we further conducted GW calculations of both quasi-particle band gap and the light absorbance as described in methods section.[35,36] Computed absorption spectra for TiNCl and TiNBr monolayers are shown in Figures 5a,b and S8, respectively. TiNCl(Br) monolayer has a quasi-particle energy gap of 2.65 (2.48) eV. Here GW correction to the PBE band gap is about 2.17 (2.00) eV. The first absorption peak corresponds to the lowest optically allowed state at 1.91 (1.82) eV (defined as the optical band gap, E_g^o) with the exciton binding energy of 0.74 (0.66) eV, see Table 1. Similar to many other 2D systems, large exciton binding energies arise from the reduced screening in the thin monolayer. Compared to the widely investigated siligraphene[50,51] and phosphorene,[52] TiNCl(Br) monolayer

Table 1. Lattice Parameters, PBE and HSE06 Gaps, Lowest Exciton Binding Energies, GW + BSE (Optical Gap, E_g^o) and G_0W_0 + RPA Gaps Calculated for TiN and TiNX (X = Cl, Br, I) Monolayers[a]

compound	TiN	TiNCl	TiNBr	TiNI
lattice $a(b)$	3.716 (3.945)	3.274 (3.978)	3.374 (3.975)	3.531 (3.993)
PBE gap		0.49	0.48	0.00
HSE06 gap		1.41	1.39	0.41
E_b		0.74	0.66	
E_g^o		1.91	1.82	
G_0W_0 gap		2.65	2.48	

[a]The lattice parameters are given in Å, whereas all other quantities are in eV.
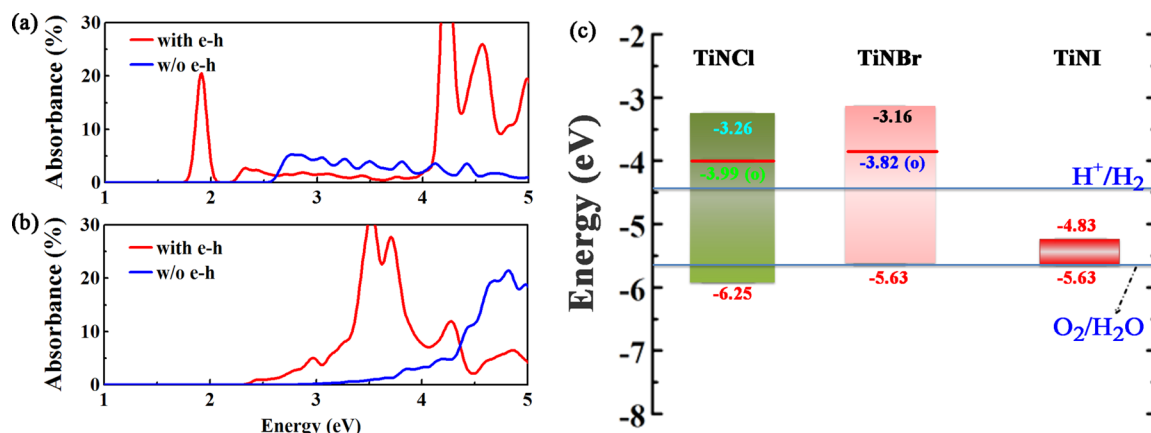
Figure 5. Absorbance spectrum of TiNCl monolayer with incident light polarized along the (a) armchair and (b) zigzag direction based on GW + RPA and GW + BSE levels. The light absorbance calculated with (without) e−h interactions are shown in blue (red). (c) Band-edge positions of the TiNX (X = Cl, Br, I) monolayers calculated at GW + RPA and GW + BSE levels is compared to the redox potentials of water. Note that due to the small energy gap of TiNI, its band-edge level is only based on the HSE06 functional. The vacuum energy level is set to 0 eV.

has decreased light absorbance at near-infrared and visible photon energies, which translates to a reduced photovoltaics potential. Nevertheless, the 1.91 and 1.82 eV band gaps are ideally suited for driving the hydrogen and oxygen reactions while ensuring the proper solar light absorption. This suggests potential photocatalytic water splitting application. Subsequently, we calculated the absolute values of TiNCl(Br) monolayer band edges (the conduction band minimum (CBM) and valence band maximum (VBM)) to compare them to the redox potentials of water, that is, the reduction potential of H^+/H_2 (−4.44 eV) and the oxidation potential of O_2/H_2O (−5.67 eV). It is noteworthy that in photocatalytic water-splitting, the exciton first diffuses to the solid/water interface and further dissociates into an unbound electron and hole.[53] To ensure this hydrogen reduction reaction, both the CBM determined from the single-particle energies at GW + RPA level and the optical CBM from GW + BSE calculations should be higher than the reduction potential of H^+/H_2. Otherwise, the excited electron is inclined to recombine with the holes in valence bands. Thus, we consider the exciton binding energy to guarantee the optical band-edge positions' matching with the reduction potential of hydrogen reduction.

The relative estimated band alignments of TiNX (X = Cl, Br, and I) monolayers are shown in Figure 5c. We find that the optical band-edge positions of TiNCl perfectly straddle the redox potentials of water, suggesting potential application for photocatalytic water splitting. As for TiNBr monolayer, the optical CBM of TiNBr monolayer is high enough to drive the kinetics of hydrogen evolution, whereas the VBM is almost the same to the oxidation potential of O_2/H_2O, implying somewhat limited capacity to split water. Notably, our estimates imply PH = 0. Tuning the PH value and an appropriate strain engineering could enable a better match to the redox potentials of water for both materials considered. In contrast, the TiNI is not suitable for these applications due to its semimetal features. Finally, we note that presented computational data for TiNCl and TiNBr monolayers substantially differ from previous estimates based on HSE06 level.[17] The underlining reason for such a difference is inclusion of electron−hole correlations and the reduced charge screening effect in these 2D systems accounted by GW approach in our simulations.

In summary, using first-principles calculations we study energetically and thermally stable rectangular TiN monolayer constructing by tetra-coordinated N and six-coordinated Ti atoms. Structurally, its lattice is comprised of two Ti—N chains linked by intra- and interchain Ti—N bonds with strong in-plane d−p orbital hybridization and synergetic out-of-plane electronic delocalization. Our simulations predict auxeticity and ferroelasticity for TiN monolayer, which are yet to be observed in other transition-metal-based 2D materials. Specifically, the ferroelastic lattice rotation produces a strain-driven lattice switch, and competitive interactions within intra- and inter- Ti—N chains lead to the appearance of alternating order of Possion's ratios. The latter implies potential applications of TiN nanosystems in the fields of high energy absorption and fracture resistance. Electronically, the TiN monolayer is a n-type metallic conductor with a significant pseudogap in the band structure. Our simulations demonstrate that halogenation of TiN sheet downshifts the Fermi level, achieving the optical energy gap of 1.91 and 1.82 eV for TiNCl and TiNBr monolayers, respectively. Our comparisons of the calculated band-edge positions with the redox potentials of water suggest the potential application of these two materials for photocatalytic water splitting. These appealing mechanical, electronic, and optical properties render TiN nanosystems as promising materials for a variety of future technological uses. Our modeling results are expected to facilitate fabrication and synthetic efforts in the area of 2D transition-metal-based systems guiding experiments toward desired functionalities in these advanced materials.

■ ASSOCIATED CONTENT

Ⓢ Supporting Information

The Supporting Information is available free of charge on the ACS Publications website at DOI: 10.1021/acs.nanolett.7b01704.

The atomistic structure of hexagonal and plane square TiN monolayer, phonon spectrum snapshots from molecular dynamics, elastic energy under axial strain, variations of total energies, band structures of TiNX (X = Cl, Br, I) monolayers, and absorbance of TiNBr monolayer (PDF)

■ AUTHOR INFORMATION

Corresponding Authors

*(L.Z.): Email: ljzhou86@lanl.gov.
*(S.T.): E-mail: serg@lanl.gov.

ORCID ⦾

Liujiang Zhou: 0000-0001-5814-4486
Liangzhi Kou: 0000-0002-3978-117X
Aijun Du: 0000-0002-3369-3283
Sergei Tretiak: 0000-0001-5547-3647

Notes

The authors declare no competing financial interest.

◼ REFERENCES

(1) Wang, Q. H.; Kalantar-Zadeh, K.; Kis, A.; Coleman, J. N.; Strano, M. S. *Nat. Nanotechnol.* **2012**, *7*, 699−712.

(2) Chhowalla, M.; Shin, H. S.; Eda, G.; Li, L.-J.; Loh, K. P.; Zhang, H. *Nat. Chem.* **2013**, *5*, 263−275.

(3) Lv, R.; Robinson, J. A.; Schaak, R. E.; Sun, D.; Sun, Y.; Mallouk, T. E.; Terrones, M. *Acc. Chem. Res.* **2015**, *48*, 56−64.

(4) Mak, K. F.; Lee, C.; Hone, J.; Shan, J.; Heinz, T. F. *Phys. Rev. Lett.* **2010**, *105*, 136805.

(5) Xu, M.; Liang, T.; Shi, M.; Chen, H. *Chem. Rev.* **2013**, *113*, 3766−3798.

(6) Li, J.; Gao, G.; Min, Y.; Yao, K. *Phys. Chem. Chem. Phys.* **2016**, *18*, 28018−28023.

(7) Wu, F.; Huang, C.; Wu, H.; Lee, C.; Deng, K.; Kan, E.; Jena, P. *Nano Lett.* **2015**, *15*, 8277−8281.

(8) Wang, Y.; Wang, S.-S.; Lu, Y.; Jiang, J.; Yang, S. A. *Nano Lett.* **2016**, *16*, 4576−4582.

(9) Wang, S.; et al. *J. Am. Chem. Soc.* **2015**, *137*, 4815−4822.

(10) Liu, P.-F.; Zhou, L.; Frauenheim, T.; Wu, L.-M. *Nanoscale* **2017**, *9*, 1007−1013.

(11) Anand, S.; Thekkepat, K.; Waghmare, U. V. *Nano Lett.* **2016**, *16*, 126−131.

(12) Kuklin, A. V.; Kuzubov, A. A.; Kovaleva, E. A.; Mikhaleva, N. S.; Tomilin, F. N.; Lee, H.; Avramov, P. V. *Nanoscale* **2017**, *9*, 621−630.

(13) Liu, J.; Li, X.-B.; Zhang, W.-J.; Yin, W.-J.; Zhang, H.-B.; Peng, P.; Liu, L.-M. L. *J. Appl. Phys.* **2014**, *115*, 093504.

(14) Zhou, L.; Shao, B.; Shi, W.; Sun, Y.; Felser, C.; Yan, B.; Frauenheim, T. *2D Mater.* **2016**, *3*, 035022.

(15) Zhang, Z.; Liu, X.; Yakobson, B. I.; Guo, W. *J. Am. Chem. Soc.* **2012**, *134*, 19326−19329.

(16) Wang, A.; Wang, Z.; Du, A.; Zhao, M. *Phys. Chem. Chem. Phys.* **2016**, *18*, 22154−22159.

(17) Liu, J.; Li, X.-B.; Wang, D.; Liu, H.; Peng, P.; Liu, L.-M. *J. Mater. Chem. A* **2014**, *2*, 6755−6761.

(18) Zhou, L.; Shi, W.; Sun, Y.; Shao, B.; Felser, C.; Yan, B.; Frauenheim, T. *2D Mater.* **2016**, *3*, 035018.

(19) Jiang, J.-W.; Park, H. S. *Nat. Commun.* **2014**, *5*, 4727.

(20) Wang, H.; Li, X.; Li, P.; Yang, J. *Nanoscale* **2017**, *9*, 850−855.

(21) Zhang, L.-C.; Qin, G.; Fang, W.-Z.; Cui, H.-J.; Zheng, Q.-R.; Yan, Q.-B.; Su, G. *Sci. Rep.* **2016**, *6*, 19830.

(22) Kou, L.; Ma, Y.; Tang, C.; Sun, Z.; Du, A.; Chen, C. *Nano Lett.* **2016**, *16*, 7910−7914.

(23) Jiang, J.-W.; Park, H. S. *Nano Lett.* **2016**, *16*, 2657−2662.

(24) Zhang, S.; Zhou, J.; Wang, Q.; Chen, X.; Kawazoe, Y.; Jena, P. *Proc. Natl. Acad. Sci. U. S. A.* **2015**, *112*, 2372−2377.

(25) Wang, Y.; Li, F.; Li, Y.; Chen, Z. *Nat. Commun.* **2016**, *7*, 11488.

(26) Yagmurcukardes, M.; Sahin, H.; Kang, J.; Torun, E.; Peeters, F.; Senger, R. *J. Appl. Phys.* **2015**, *118*, 104303.

(27) Gao, Z.; Dong, X.; Li, N.; Ren, J. *Nano Lett.* **2017**, *17*, 772−777.

(28) Wu, M.; Zeng, X. C. *Nano Lett.* **2016**, *16*, 3236−3241.

(29) Kresse, G.; Furthmüller, J. *Phys. Rev. B: Condens. Matter Mater. Phys.* **1996**, *54*, 11169−11186.

(30) Perdew, J. P.; Burke, K.; Ernzerhof, M. *Phys. Rev. Lett.* **1996**, *77*, 3865−3868.

(31) Perdew, J. P.; Zunger, A. *Phys. Rev. B: Condens. Matter Mater. Phys.* **1981**, *23*, 5048−5079.

(32) Heyd, J.; Scuseria, G. E.; Ernzerhof, M. *J. Chem. Phys.* **2006**, *124*, 219906.

(33) Heyd, J.; Scuseria, G. E.; Ernzerhof, M. *J. Chem. Phys.* **2003**, *118*, 8207−8215.

(34) Togo, A.; Tanaka, I. *Scr. Mater.* **2015**, *108*, 1−5.

(35) Rohlfing, M.; Louie, S. G. *Phys. Rev. B: Condens. Matter Mater. Phys.* **2000**, *62*, 4927−4944.

(36) Deslippe, J.; Samsonidze, G.; Strubbe, D. A.; Jain, M.; Cohen, M. L.; Louie, S. G. *Comput. Phys. Commun.* **2012**, *183*, 1269−1289.

(37) Ismail-Beigi, S. *Phys. Rev. B: Condens. Matter Mater. Phys.* **2006**, *73*, 233103.

(38) Hybertsen, M. S.; Louie, S. G. *Phys. Rev. B: Condens. Matter Mater. Phys.* **1986**, *34*, 5390−5413.

(39) Cahangirov, S.; Topsakal, M.; Aktürk, E.; Şahin, H.; Ciraci, S. *Phys. Rev. Lett.* **2009**, *102*, 236804.

(40) Molina-Sánchez, A.; Wirtz, L. *Phys. Rev. B: Condens. Matter Mater. Phys.* **2011**, *84*, 155413.

(41) Henkelman, G.; Arnaldsson, A.; Jónsson, H. *Comput. Mater. Sci.* **2006**, *36*, 354−360.

(42) Zhang, S.; Wang, Q.; Kawazoe, Y.; Jena, P. *J. Am. Chem. Soc.* **2013**, *135*, 18216−18221.

(43) Lee, C.; Wei, X.; Kysar, J. W.; Hone, J. *Science* **2008**, *321*, 385−388.

(44) Castellanos-Gomez, A.; Poot, M.; Steele, G. A.; van der Zant, H. S. J.; Agraït, N.; Rubio-Bollinger, G. *Adv. Mater.* **2012**, *24*, 772−775.

(45) Zhuo, Z.; Wu, X.; Yang, J. *J. Am. Chem. Soc.* **2016**, *138*, 7091−7098.

(46) Zhao, S.; Li, Z.; Yang, J. *J. Am. Chem. Soc.* **2014**, *136*, 13313−13318.

(47) Topsakal, M.; Ciraci, S. *Phys. Rev. B: Condens. Matter Mater. Phys.* **2010**, *81*, 024107.

(48) Qin, R.; Zheng, J.; Zhu, W. *Nanoscale* **2017**, *9*, 128−133.

(49) Juza, R.; Heners, J. *Z. Anorg. Allg. Chem.* **1964**, *332*, 159−172.

(50) Zhou, L.-J.; Zhang, Y.-F.; Wu, L.-M. *Nano Lett.* **2013**, *13*, 5431−5436.

(51) Dong, H.; Zhou, L.; Frauenheim, T.; Hou, T.; Lee, S.-T.; Li, Y. *Nanoscale* **2016**, *8*, 6994−6999.

(52) Zhou, L.; Zhang, J.; Zhuo, Z.; Kou, L.; Ma, W.; Shao, B.; Du, A.; Meng, S.; Frauenheim, T. *J. Phys. Chem. Lett.* **2016**, *7*, 1880−1887.

(53) Singh, A. K.; Mathew, K.; Zhuang, H. L.; Hennig, R. G. *J. Phys. Chem. Lett.* **2015**, *6*, 1087−1098.